

Atomically dispersed Cu coordinated Rh metallene arrays for simultaneously electrochemical aniline synthesis and biomass upgrading

Received: 8 May 2023

Accepted: 1 September 2023

Published online: 14 September 2023

 Check for updatesQiqi Mao¹, Xu Mu¹, Wenxin Wang¹, Kai Deng¹, Hongjie Yu¹, Ziqiang Wang¹, You Xu¹, Liang Wang¹ & Hongjing Wang¹ 

Organic electrocatalytic conversion is an essential pathway for the green conversion of low-cost organic compounds to high-value chemicals, which urgently demands the development of efficient electrocatalysts. Here, we report a Cu single-atom dispersed Rh metallene arrays on Cu foam for cathodic nitrobenzene electroreduction reaction and anodic methanol oxidation reaction. In the coupled electrocatalytic system, the Cu_{single-atom}-Rh metallene arrays on Cu foam requires only the low voltages of 1.18 V to reach current densities of 100 mA cm⁻² for generating aniline and formate, with up to -100% of nitrobenzene conversion/ aniline selectivity and over -90% of formate Faraday efficiency, achieving synthesis of high-value chemicals. Density functional theory calculations reveal the electron effect between Cu single-atom and Rh host and catalytic reaction mechanism. The synergistic catalytic effect and H*-spillover effect can improve catalytic reaction process and reduce energy barrier for reaction process, thus enhancing electrocatalytic reaction activity and target product selectivity.

The utilization of renewable energy is a crucial pathway for solving the increasing energy crisis and promoting the green low-carbon transformation of energy^{1,2}. The organic electrocatalytic conversion, driven by electricity generated from renewable energy sources at ambient temperature and pressure^{3,4}, is a green synthesis route for achieving controlled conversion of low-cost organic compounds into high-value chemicals and holds considerable research significance and application potential in the chemical industry and organic synthesis⁵⁻⁷. Among the numerous organic electrocatalytic conversion reactions, the cathodic nitrobenzene (Ph-NO₂) electroreduction for aniline (Ph-NH₂) synthesis is regarded as a more low-carbon and environment-friendly green Ph-NH₂ synthesis process using H₂O and electrons as the hydrogen source and reductant, compared with high pollution and harsh conditions of traditional chemical synthesis method⁸⁻¹¹. Notably,

the anodic reaction for the conventional cathodic Ph-NO₂ electroreduction reaction (Ph-NO₂ ERR) is a sluggish kinetic oxygen evolution reaction (OER)^{12,13}. In contrast, the anodic biomass electrooxidation reaction not only can achieve the upgrading of cheap biomass but also offers the advantages of low energy consumption and high electrolysis efficiency¹⁴⁻¹⁶. Currently, the cheap and widespread methanol (CH₃OH, 350 USD/t) is considered an appropriate precursor for the high-value formate (HCOO⁻, 1300 USD/t) synthesis via anodic electrooxidation reaction^{17,18}, and methanol electrooxidation reaction (MOR) coupled with various electrocatalytic reactions has attracted widespread research interest worldwide^{19,20}. In view of this, the construction of Ph-NO₂ ERR-MOR coupled electrolytic system is a promising strategy for achieving high-value chemical synthesis from sustainable organic electrocatalytic conversion. Nevertheless, both Ph-NO₂-to-Ph-NH₂ and

¹State Key Laboratory Breeding Base of Green-Chemical Synthesis Technology, College of Chemical Engineering, Zhejiang University of Technology, Hangzhou 310014, P. R. China. ✉e-mail: hjw@zjut.edu.cn

methanol-to-formate are multi-step reaction processes and are limited by numerous side reactions^{21,22}. To address these bottlenecks, it is fundamental to explore efficient bifunctional electrocatalysts for activating reaction pathways of the directed synthesis towards Ph-NH₂ and formate.

Recently, the single-atom alloys (SAAs) catalysts, consisting of exogenous isolated metal atoms dispersed on the surface of the metal host^{23,24}, as a promising material with the advantages of high active atom utilization of single-atom catalysts (SACs) and alloy synergistic effect^{25,26}, have been in the field of various electrocatalytic energy conversions^{27–30}. For example, Duan and co-workers designed a Ru₁Cu SAAs with isolated Ru atoms on Cu nanowires for the electrocatalytic conversion of 5-hydroxymethylfurfural (HMF) to 2,5-dihydroxymethylfuran (DHMF), where the introduction of Ru single-atom sites facilitates the dissociation of H₂O to produce H* species for the HMF hydrogenation process³¹. Thus, the electron effect and metal-support interaction of SAAs can promote effective dissociation of reactants and optimize the adsorption/desorption of key intermediates to achieve an optimum balance between reactants and intermediates, leading to high activity and selectivity^{32,33}. Furthermore, the electrocatalytic activity of SAAs catalysts can be further improved by the precise regulation for morphology and structure^{34,35}. Metallene, a group of graphene-like two-dimensional (2D) nanomaterials with a thickness less than 5 nm^{36,37}. Due to their flexible microstructural tunability, highly exposed metal active sites as well as simple and well-defined structure model^{38,39}, metallene can serve as a desirable carrier for immobilizing single-atom, clusters, or nanoparticles, which has attracted great research interest^{40,41}. For example, Xiaoqiang Cui et al. report a dispersed MoO_x on Rh metallene (MoO_x-Rh metallene) for boosting alkaline HER⁴². Chu's group prepare a single-atom Bi alloyed Pd metallene (Bi₁Pd metallene) that shows excellent NO₃⁻ electroreduction reaction activity and near 100% Faradaic efficiency of NH₃⁴³. Therefore, the design and development of SAA metallene are extremely promising for improving electrocatalytic activity and catalytic product selectivity.

In this work, we report a synthesis of Cu single-atom dispersed Rh metallene arrays on Cu foam (Cu_{SA}-Rh MAs/CF) by a facile and rapid one-step solvothermal approach. As a bifunctional electrocatalyst, the Cu_{SA}-Rh MAs/CF displays superior electrocatalytic activity for Ph-NO₂ ERR and MOR. For the constructed Ph-NO₂ ERR-MOR coupled electrocatalytic system, the low voltage of only 1.05/1.18 V achieves current densities of 50/100 mA cm⁻² for efficient conversion of Ph-NO₂-to-Ph-NH₂ and methanol-to-formate, with Ph-NO₂ conversion and Ph-NH₂ selectivity up to -100% and HCOO⁻ FE reaching over -90% on Cu_{SA}-Rh MAs/CF, which not only enables the simultaneous cathodic and anodic organic electrocatalytic conversion for the synthesis of high-value chemicals but also maximizes the energy efficiency. Moreover, density functional theory (DFT) calculations further reveal the synergistic catalysis effect and H*-spillover effect induced by the local electron change between the isolated Cu single-atom and the Rh host, which promotes the rapid conversion of the reactants to key intermediates and rapid desorption of the target products thus enhancing electrocatalytic reaction activity and targeted product selectivity.

Results

Synthesis and characterization of Cu_{SA}-Rh MAs/CF

The Cu_{SA}-Rh MAs/CF was synthesized using a straightforward one-step solvothermal method (Supplementary Fig. 1), which contains rhodium (II) acetate dimer (C₈H₁₂O₈Rh₂), N,N-dimethylformamide (DMF), potassium hydroxide (KOH), ethylene glycol (EG), diethylenetriamine (DETA) and CF as reactants. In this synthesis process, the formed DMA by the synergistic interaction of DMF and KOH can induce the 2D nanosheet structure growth by facet control as well as diamine ligand DETA can chelate with metal ions to reduce the metal reduction rate thus promoting the formation of 2D nanosheet structure⁴⁴.

Supplementary Fig. 2 shows that the surface color of formed Cu_{SA}-Rh MAs/CF is black, which is significantly different from that of CF. Figure 1a displays uniform ultrathin nanosheets grown on the CF surface to form metallene arrays, and the nanosheets are tightly interconnected to each other to form a security wall-like structure, which contributes to providing enough active sites as well as facilitating rapid charge transfer and mass transfer during the electrocatalysis process⁴⁵. Transmission electron microscopy (TEM) images of Cu_{SA}-Rh MAs further display the ultrathin nanosheet-like metallene structure with lateral dimensions of around several hundred nanometers (Fig. 1b). The thickness of a single nanosheet in Cu_{SA}-Rh MAs was measured to be ~1.51 nm corresponding to 7–8 atomic layers (Fig. 1c and Supplementary Fig. 3), further proving the ultrathin nature for Cu_{SA}-Rh MAs. The ultrathin 2D nanosheet structure with certain curvature can provide highly accessible surface atoms, highly exposed active sites, and rich defect structures, which is conducive to promoting the electrocatalytic process³⁷. Figure 1d presents the aberration-corrected high-angle annular dark field scanning transmission electron microscopy (AC-HAADF-STEM) and corresponding elemental mapping images of Cu_{SA}-Rh MAs, revealing the homogeneous distribution of Cu atoms in Cu_{SA}-Rh MAs. The Rh/Cu atomic ratio was further determined to be approximately 93.6/6.4 via the TEM energy dispersive X-ray spectroscopy (TEM-EDS, Supplementary Fig. 4). The mass ratio (Rh/Cu = 95.1/4.9) and atomic ratio (Rh/Cu = 92.6/7.4) of Rh/Cu in Cu_{SA}-Rh MAs were further analyzed by inductively coupled plasma optical emission spectroscopy (ICP-OES) (Supplementary Fig. 5), which is close to the results obtained from TEM-EDS. Furthermore, as revealed by the electron energy loss spectrum (EELS) of Cu_{SA}-Rh MAs (Supplementary Fig. 6), the energy loss peak around 498.8 eV can be assigned to the Rh M electron transition (Supplementary Fig. 6a)^{46,47}, and the energy loss peak around 933.1 eV in Supplementary Fig. 6b can be assigned to the Cu L electron transition⁴⁸. The EELS data of Cu_{SA}-Rh MAs further reveal the existence of Rh and Cu elements. The AC-HAADF-STEM images of Cu_{SA}-Rh MAs were collected and analyzed for further investigating its structure at the atomic scale. As shown in Fig. 1e–f, the obvious vacancy defects are observed on the basal surface of Cu_{SA}-Rh MAs and the presence of atomic vacancies is also verified by the corresponding integrated pixel intensity profile in the red region of Fig. 1e. Moreover, the lattice spacing (*d* = 0.220 nm) of Cu_{SA}-Rh MAs can be indexed to the typical face-centered cube (fcc) Rh (111) facet and the appearance of amorphous sites in Cu_{SA}-Rh MAs reveals the presence of crystalline and amorphous phases (Fig. 1g). In the X-ray diffraction (XRD) pattern (Fig. 1h), the characteristic peaks of Cu_{SA}-Rh MAs can be assigned to a typical fcc metallic Rh phase (No. 05–0685). Notably, the characteristic peaks of Cu_{SA}-Rh MAs exhibit a negative shift compared with the Rh JCPDS card, originating from the curved 2D geometrical structure and the introduction of Cu atoms³⁸. Moreover, the poor crystallinity is revealed by the weak and broad characteristic peaks of Cu_{SA}-Rh MAs in consistent with the selected area electron diffraction (SAED, inset in Fig. 1h) result, which further indicates the presence of the crystalline and amorphous phases in Cu_{SA}-Rh MAs. In detail, the vacancy defects and amorphous sites as highly active low-coordination sites can break the inherent crystal arrangement to cause atomic unsaturated bonding and readjust the local electron structure for optimizing the surface electron structure of the electrocatalyst, which is beneficial for improving the electrocatalytic activity³⁷. The Cu single-atom was analyzed by AC-HAADF-STEM image and 3D topographic atom images. Figure 2a shows that some individual dark dots (Cu atoms) can be observed on the surface of Cu_{SA}-Rh MAs owing to the lower atomic number of Cu (29) compared with Rh (45). The low-intensity dots also indicate the dispersion situation of the isolated Cu atoms on the surface of Cu_{SA}-Rh MAs (Fig. 2b, c). The corresponding integrated pixel intensity profile also illustrates the isolated low-intensity Cu atoms dispersed surrounding the high-intensity Rh atoms on the crystal surface (Fig. 2d), further proving the presence of isolated Cu

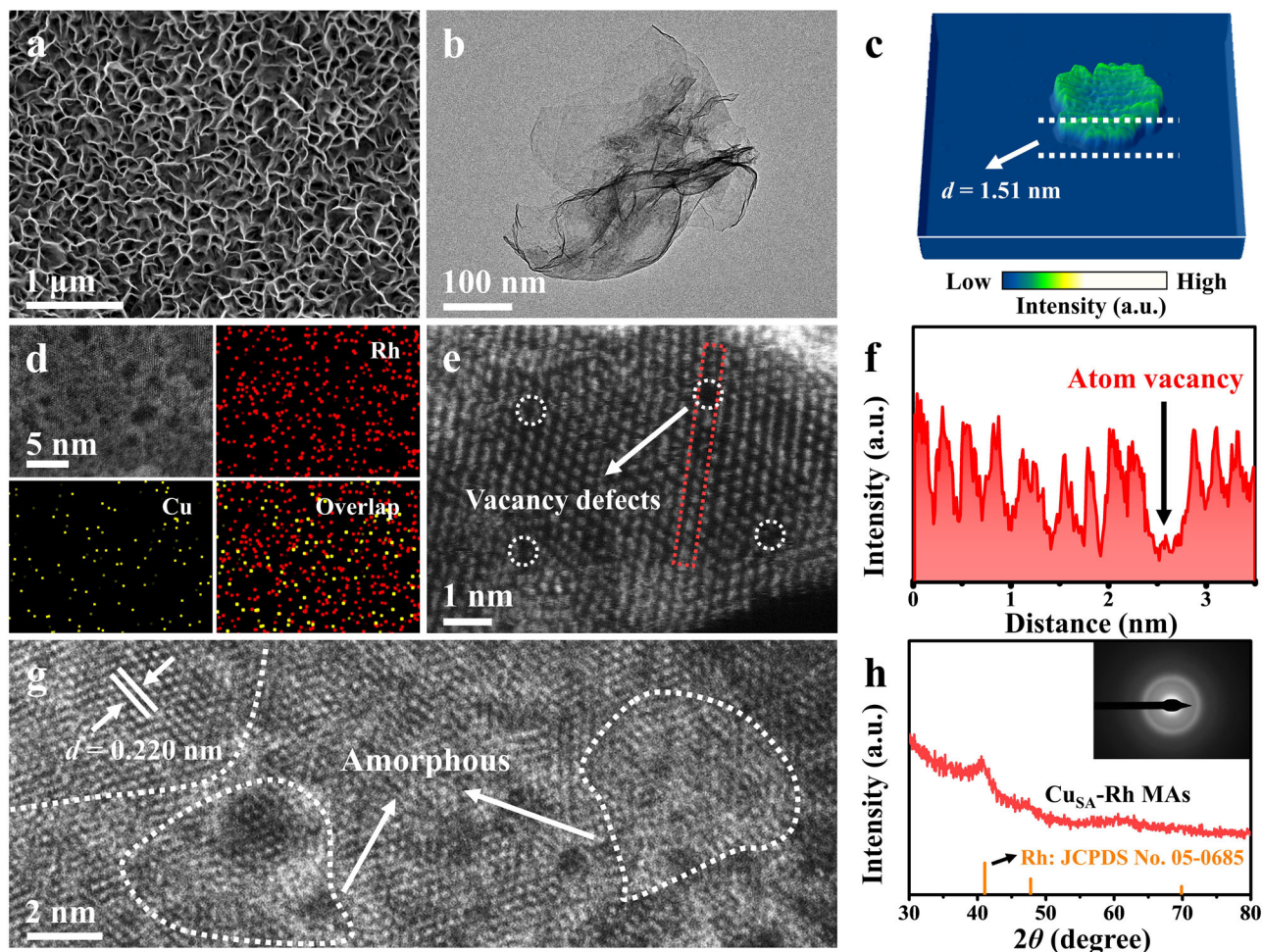


Fig. 1 | Morphological and structure characterization of $\text{Cu}_{\text{SA}}\text{-Rh MAs/CF}$. **a** SEM image of $\text{Cu}_{\text{SA}}\text{-Rh MAs/CF}$. **b** TEM image, **c** 3D view for the corresponding AFM image, **d** AC-HAADF-STEM image, and the corresponding elemental mapping images of $\text{Cu}_{\text{SA}}\text{-Rh MAs}$. **e** AC-HAADF-STEM image of $\text{Cu}_{\text{SA}}\text{-Rh MAs}$. **f** The integrated

pixel intensity profile for the selected red region in **e**. **g** AC-HAADF-STEM image of $\text{Cu}_{\text{SA}}\text{-Rh MAs}$. **h** XRD pattern of $\text{Cu}_{\text{SA}}\text{-Rh MAs}$ and the inset in **h** displays the corresponding SAED pattern of $\text{Cu}_{\text{SA}}\text{-Rh MAs}$.

single-atom on the $\text{Cu}_{\text{SA}}\text{-Rh MAs}$. The strong metallic interaction between the isolated Cu single-atom and Rh metallene support can modulate the electronic structure of active sites and form the activated Rh-coordinated Cu single-atom active sites, which is beneficial for optimizing the adsorption and activation between active sites and reactants during electrocatalytic reactions^{25,43}.

The elemental composition, chemical valence, and coordination environment for $\text{Cu}_{\text{SA}}\text{-Rh MAs}$ were investigated through the X-ray photoelectron spectroscopy (XPS), X-ray absorption near-edge structure (XANES), and extended X-ray absorption fine structure (EXAFS) tests. As shown in Fig. 2e, the Rh 3d spectrum of $\text{Cu}_{\text{SA}}\text{-Rh MAs}$ reveals that four obvious characteristic peaks (307.42 eV, 308.75 eV, 312.19 eV, 313.98 eV) are ascribed to $\text{Rh}^0 3d_{5/2}$, $\text{Rh}^{3+} 3d_{5/2}$, $\text{Rh}^0 3d_{3/2}$ and $\text{Rh}^{3+} 3d_{3/2}$, respectively^{46,49}, indicating the presence of Rh in $\text{Cu}_{\text{SA}}\text{-Rh MAs}$ primarily as the metallic state. In the Cu 2p spectrum of $\text{Cu}_{\text{SA}}\text{-Rh MAs}$ (Fig. 2f), two obvious characteristic peaks are at 932.50 eV and 952.37 eV ascribed to $\text{Cu}^{0/1}$, and other characteristic peaks at 934.76 eV, 954.49 eV and 942.21 eV can be ascribed to Cu^{2+} and satellite peak⁵¹. As observed from Rh K-edge XANES, EXAFS, and wavelet transform (WT) spectra (Fig. 2g–i), the similar features of $\text{Cu}_{\text{SA}}\text{-Rh MAs}$ with Rh foil reveal that the surface valence and coordination structure of Rh is not significantly changed by the introduction of Cu single-atom. Notably, based on the WT spectra analysis for $\text{Cu}_{\text{SA}}\text{-Rh MAs}$ and Rh foil (Fig. 2i), the Rh-Rh/Cu-Rh intensity maximum of $\text{Cu}_{\text{SA}}\text{-Rh MAs}$ exhibits a negative shift of -0.33 \AA^{-1} compared with Rh-Rh

intensity maximum of Rh foil, which is induced by the coordination of the Cu-Rh bond. Supplementary Figs. 7–9 shows the Rh K-edge experimental and fitting Fourier-transformed EXAFS spectra for $\text{Cu}_{\text{SA}}\text{-Rh MAs}$, Rh foil, and Rh_2O_3 , indicating a good fitting result. The Cu K-edge XANES spectra indicate that the absorption edge of $\text{Cu}_{\text{SA}}\text{-Rh MAs}$ is positioned between Cu foil and CuO (Fig. 2j), indicating an increase in the valence state of Rh for $\text{Cu}_{\text{SA}}\text{-Rh MAs}$ owing to the electron transfer from Cu to Rh. This phenomenon reveals the electronic interaction between Cu single-atom and Rh in $\text{Cu}_{\text{SA}}\text{-Rh MAs}$. The Cu K-edge EXAFS spectra show the distinct peak of $\text{Cu}_{\text{SA}}\text{-Rh MAs}$ at 2.43 \AA ascribed to the Cu-Rh bond, obviously distinct with Cu-Cu (2.23 \AA) and CuO (1.51 \AA) bands (Fig. 2k), revealing the presence of dispersed Cu single-atom. The atomically distributed Cu atoms were also identified based on the fitting results (Supplementary Figs. 10–12 and Supplementary Table 1). As displayed in Fig. 2l, The WT spectra for $\text{Cu}_{\text{SA}}\text{-Rh MAs}$, Rh foil, and Rh_2O_3 further indicate the presence of isolated Cu single-atom, where the intensity maximum (-10.31 \AA^{-1}) of $\text{Cu}_{\text{SA}}\text{-Rh MAs}$ is ascribed to the Cu-Rh bond compared with Cu-Cu (-8.01 \AA^{-1}) and CuO (-6.76 \AA^{-1}) intensity maximums.

Electrocatalytic performance for Ph- NO_2 ERR

The cathodic electrochemical Ph- NH_2 synthesis activity of $\text{Cu}_{\text{SA}}\text{-Rh MAs/CF}$ was evaluated in an H-type electrolyzer separated via a Nafion membrane under ambient conditions, consisting of a working electrode (prepared electrocatalysts), a reference electrode (Hg/HgO

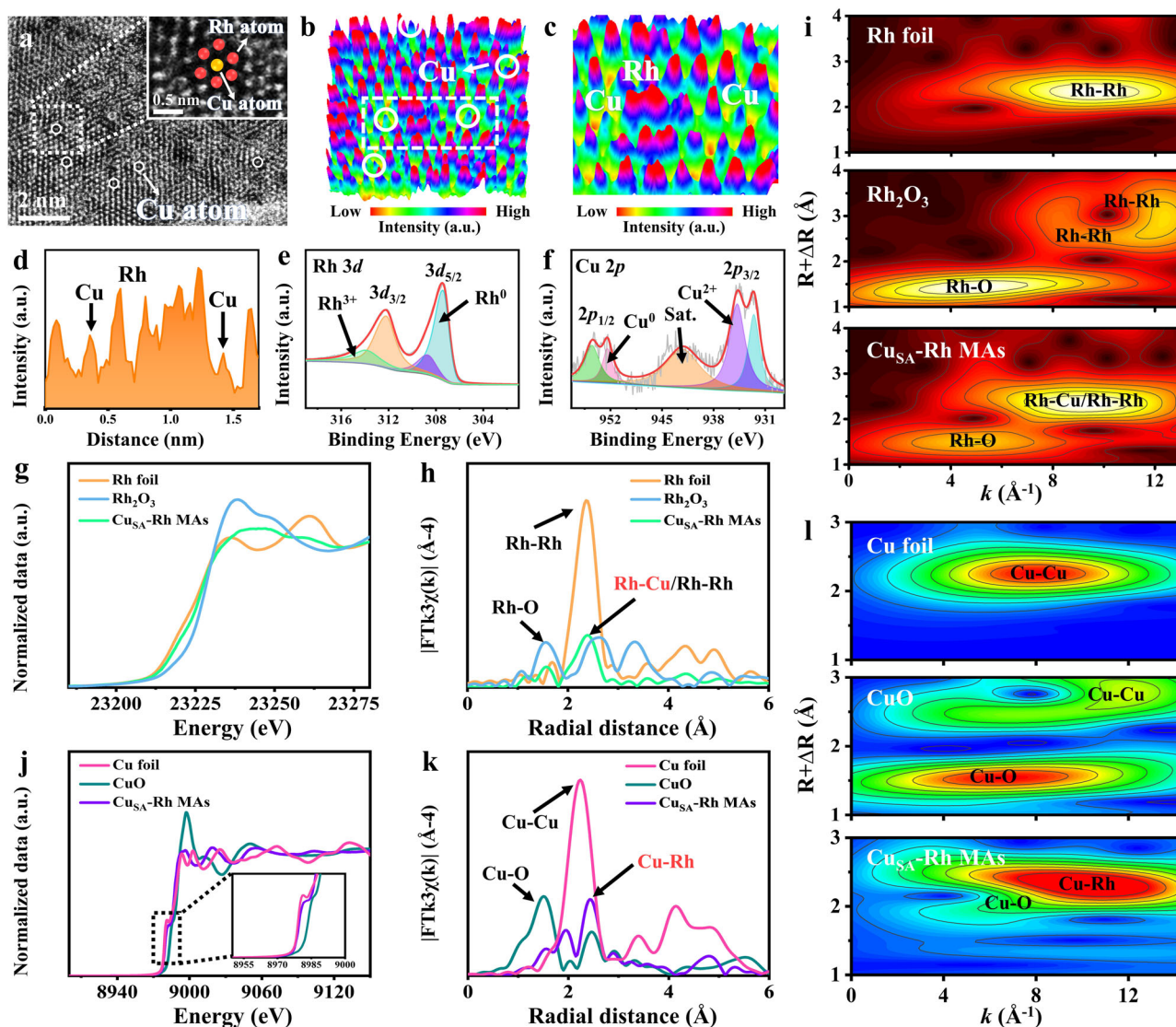


Fig. 2 | Structure characterization of $\text{Cu}_{\text{SA}}\text{-Rh MAs/CF}$. **a** AC-HAADF-STEM image of $\text{Cu}_{\text{SA}}\text{-Rh MAs}$ and the inset in **a** displays the magnified image of the selected white region in **a**. **b**, **c** 3D topographic atom images of $\text{Cu}_{\text{SA}}\text{-Rh MAs}$. **d** The integrated pixel intensity profile for the selected region in **b**. **e** Rh $3d$ XPS and **f** Cu $2p$ XPS

spectra of $\text{Cu}_{\text{SA}}\text{-Rh MAs}$. **g** Rh K -edge XANES spectra, **h** Fourier transformed EXAFS spectra and **i** EXAFS wavelet transform diagrams of Rh foil, Rh_2O_3 , and $\text{Cu}_{\text{SA}}\text{-Rh MAs}$. **j** Cu K -edge XANES spectra, **k** Fourier transformed EXAFS spectra, and **l** EXAFS wavelet transform diagrams of Cu foil, CuO, and $\text{Cu}_{\text{SA}}\text{-Rh MAs}$.

electrode) and a counter electrode (Pt foil). As shown in Fig. 3a, linear sweep voltammetry (LSV) curves of $\text{Cu}_{\text{SA}}\text{-Rh MAs/CF}$ were recorded in 1M KOH and 1M KOH + 5 mM Ph- NO_2 solutions. Apparently, a rapid increase in cathodic current density is observed at -0.4 V (vs RHE) in the presence of Ph- NO_2 , suggesting the proceeding of Ph- NO_2 electroreduction on $\text{Cu}_{\text{SA}}\text{-Rh MAs/CF}$. Furthermore, at the applied potential range from -0.7 to 0.5 V (vs RHE), the significantly improved overall current density and lower onset potential in a 1M KOH + 5 mM Ph- NO_2 solution further demonstrate the favorable Ph- NO_2 ERR activity on $\text{Cu}_{\text{SA}}\text{-Rh MAs/CF}$. To investigate the potential-dependent Ph- NO_2 conversion and Ph- NH_2 selectivity on $\text{Cu}_{\text{SA}}\text{-Rh MAs/CF}$, the chronoamperometric (i - t) measurements were performed at various applied potentials and the electrolyzed products were quantified by GC analysis. As shown in Fig. 3b, the Ph- NO_2 conversion of $\text{Cu}_{\text{SA}}\text{-Rh MAs/CF}$ is as high as $\sim 100\%$ at various applied potentials, revealing the superior Ph- NO_2 adsorption and electroreduction ability on $\text{Cu}_{\text{SA}}\text{-Rh MAs/CF}$. For Ph- NH_2 selectivity (Fig. 3c), the Ph- NH_2 selectivity of $\text{Cu}_{\text{SA}}\text{-Rh MAs/CF}$ gradually increases from the applied potentials of 0.2 to -0.2 V (vs RHE), and the Ph- NH_2 selectivity is calculated to be $\sim 99.7\%$ at -0.1 V (vs RHE) approaching 100% , which indicates the Ph- NO_2 can be

selectively electroreduced to Ph- NH_2 via hydrogenation using H_2O as the hydrogen source on $\text{Cu}_{\text{SA}}\text{-Rh MAs/CF}$. Notably, the low Ph- NH_2 selectivity of lower cathodic potentials can be ascribed to the weak ability of H_2O dissociation to produce active H^* , and the production of active H^* is gradually improved on $\text{Cu}_{\text{SA}}\text{-Rh MAs/CF}$ with the increase of cathodic potentials thus enhancing the Ph- NH_2 selectivity¹¹. Besides, Fig. 3d and Supplementary Fig. 13 reveal that the Ph- NO_2 can be completely converted to Ph- NH_2 as well as the high-boiling by-products are not present in the obtained electrolyte at an applied potential of -0.1 V (vs RHE), further indicating the superior activity for electrochemical Ph- NH_2 synthesis on $\text{Cu}_{\text{SA}}\text{-Rh MAs/CF}$. As revealed in Fig. 3e, f, the time-dependent conversion, and yield illustrate that the Ph- NH_2 concentration increases and the Ph- NO_2 concentration decrease over time, indicating a gradual and complete conversion of Ph- NO_2 to Ph- NH_2 on $\text{Cu}_{\text{SA}}\text{-Rh MAs/CF}$ at an applied potential of -0.1 V (vs RHE) for 1 h. To further investigate the mechanism for the improved Ph- NO_2 ERR to Ph- NH_2 activity over $\text{Cu}_{\text{SA}}\text{-Rh MAs/CF}$, several comparison experiments were carried out. LSV curves for various electrocatalysts demonstrate that the $\text{Cu}_{\text{SA}}\text{-Rh MAs/CF}$ possesses a stronger electroreduction activity compared with Rh metallene-CF

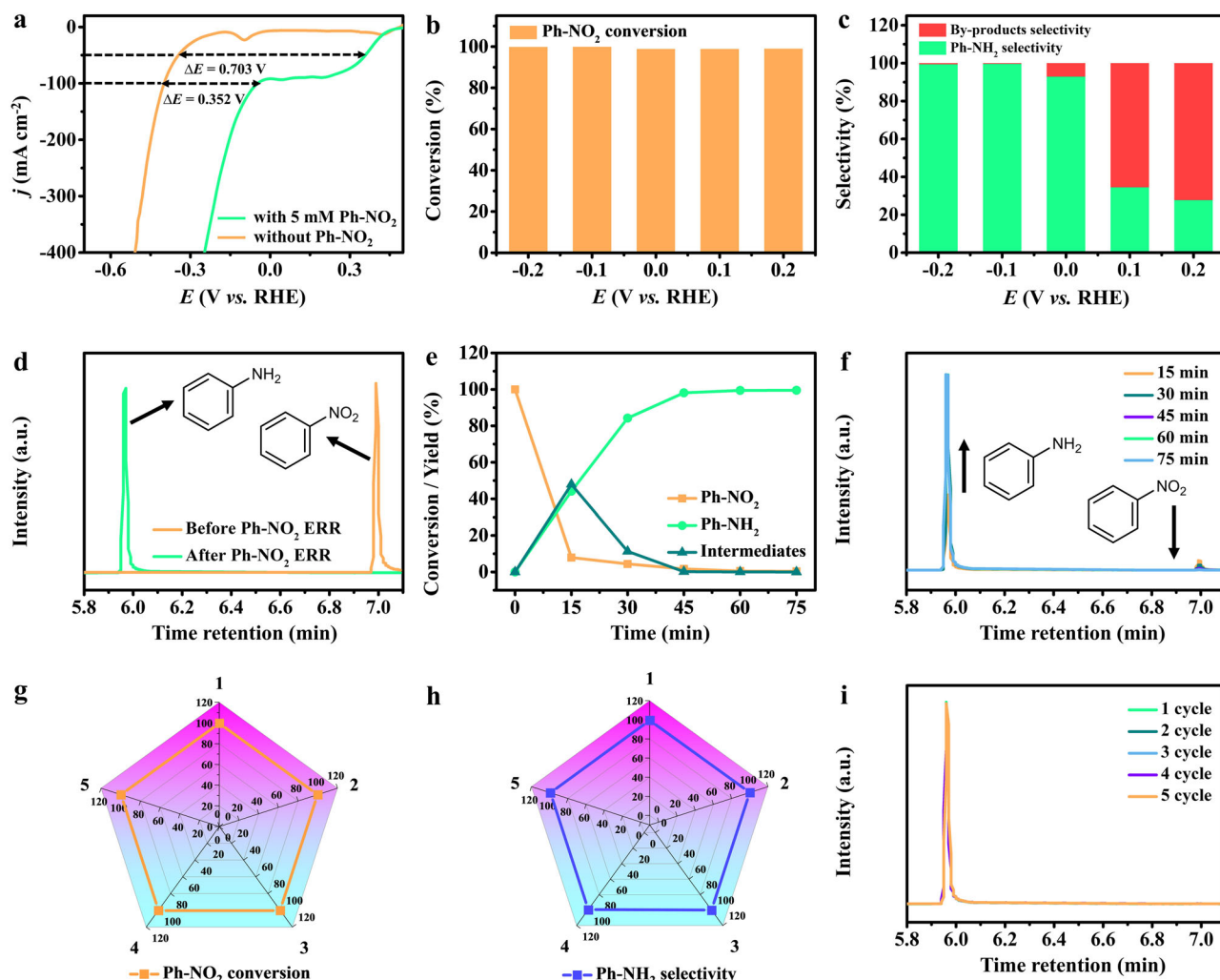


Fig. 3 | Electrochemical Ph-NO₂ ERR performance. **a** IR-corrected LSV curves for Cu_{SA}-Rh MAs/CF (catalyst loading: 2.5 mg cm⁻²) in 1 M KOH (pH = 13.9) and 1 M KOH + 5 mM Ph-NO₂ (pH = 13.7) solutions. **b** Ph-NO₂ conversion and **c** Ph-NH₂ selectivity for Cu_{SA}-Rh MAs/CF at various applied potentials in 1 M KOH + 5 mM Ph-NO₂ (pH = 13.7) solutions. **d** GC results of products before and after Ph-NO₂ ERR for

Cu_{SA}-Rh MAs/CF at -0.1 V (vs RHE). **e** Time-dependent conversion and yield for Ph-NO₂ ERR of Cu_{SA}-Rh MAs/CF. **f** GC results for Ph-NO₂ ERR of Cu_{SA}-Rh MAs/CF at -0.1 V (vs RHE) with various time. **g** Ph-NO₂ conversion, **h** Ph-NH₂ selectivity and **i** GC results for Ph-NO₂ ERR of Cu_{SA}-Rh MAs/CF at -0.1 V (vs RHE) measured for 5 successive cycles in 1 M KOH + 5 mM Ph-NO₂ (pH = 13.7) solutions.

(Rhene-CF), Rh nanoparticles-CF (Rh NPs-CF), and CF (Supplementary Fig. 14a), and the Ph-NH₂ selectivity (99.7%) of Cu_{SA}-Rh MAs/CF is much higher than those of Rhene-CF (64.7%), Rh NPs-CF (59.3%) and CF (28.3%) (Supplementary Fig. 14b). Moreover, with respect to the standard potential (0.89 V vs RHE) of the Ph-NO₂ ERR²¹, the overpotential (0.532 V vs RHE) of Cu_{SA}-Rh MAs/CF is lower than those of Rhene-CF (0.667 V vs RHE), Rh NPs-CF (0.619 V vs RHE) and CF (0.638 V vs RHE) for achieving a current density of -50 mA cm⁻² (Supplementary Fig. 15), further suggesting a superior Ph-NO₂ ERR activity on Cu_{SA}-Rh MAs/CF. The improved activity of Ph-NO₂ ERR to Ph-NH₂ for Cu_{SA}-Rh MAs/CF originates from the ultrathin metallene array structure and the synergistic effect of isolated Cu single-atom with Rh host. Moreover, the stability of electrochemical Ph-NH₂ synthesis is also a critical parameter for evaluating Ph-NO₂ ERR activity. After 5 repeated cycles of testing on Cu_{SA}-Rh MAs/CF, the decay was almost negligible for Ph-NO₂ conversion, Ph-NH₂ selectivity, and Ph-NH₂ intensity (Fig. 3g-i), revealing a superb stability for Ph-NO₂ ERR to Ph-NH₂ of Cu_{SA}-Rh MAs/CF.

Electrocatalytic performance for MOR

A single-chamber cell with a three-electrode system was utilized to investigate the anodic electrochemical methanol (CH₃OH)

upgrading for high value-added formate (HCOO⁻) production on Cu_{SA}-Rh MAs/CF. The working electrode contained prepared electrocatalysts, while Hg/HgO electrode and carbon rod served as reference electrode and counter electrode. Figure 4a displays the LSV curves of Cu_{SA}-Rh MAs/CF recorded in 1 M KOH with different CH₃OH concentrations solutions. Visibly, the Cu_{SA}-Rh MAs/CF exhibits an optimal MOR activity when the CH₃OH concentration reaches 4 M. The oxidation potentials (E_{50} , E_{100} , E_{150} , and E_{200}) of only 1.40, 1.44, 1.46, and 1.47 V (vs RHE) are required for reaching the current densities of 50, 100, 150 and 200 mA cm⁻² at a 1 M KOH + 4 M CH₃OH solution (Fig. 4b), which is lower than those of other CH₃OH concentrations. Notably, the MOR activity decays significantly when the CH₃OH concentration increases to 8 M, which can originate from the poor conductivity of the mixed solution as well as excessive oxidation species adsorbed on the active site to hinder the reaction²⁰. Hence, it is considered that a 4 M CH₃OH is appropriate for this system. Figure 4c illustrates the LSV curves of Cu_{SA}-Rh MAs/CF recorded in MOR (with 4 M CH₃OH) and OER (without 4 M CH₃OH). Obviously, the onset potential is significantly reduced after the addition of CH₃OH. The oxidation potentials (E_{50} = 1.40, E_{100} = 1.44, E_{150} = 1.46 and E_{200} = 1.47 V vs RHE) for MOR are lower than those for OER (E_{50} = 1.57, E_{100} = 1.60, E_{150} = 1.62 and E_{200} = 1.64 V

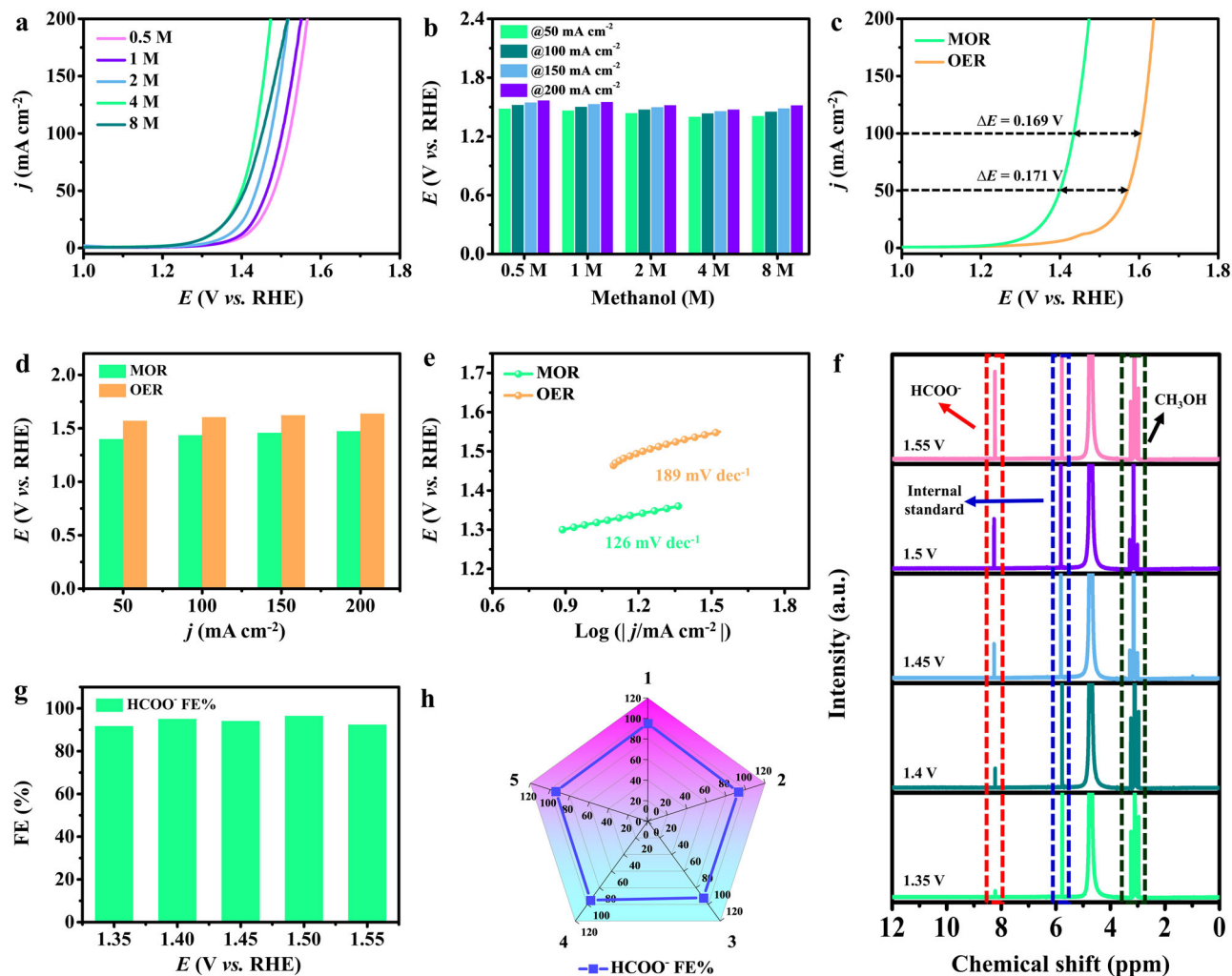


Fig. 4 | Electrochemical MOR performance. **a** IR-corrected LSV curves for $\text{Cu}_{\text{SA}}\text{-Rh MAS/CF}$ (catalyst loading: 2.5 mg cm^{-2}) and **b** corresponding overpotentials comparison at 50/100/150/200 mA cm^{-2} in 1 M KOH containing 0.5 M (pH = 13.9), 1 M (pH = 13.8), 2 M (pH = 13.8), 4 M (pH = 13.7) and 8 M (pH = 13.7) CH_3OH solutions. **c** LSV curves, **d** corresponding overpotentials comparison at 50/100/150/200 mA cm^{-2} and **e** Tafel plots of $\text{Cu}_{\text{SA}}\text{-Rh MAS/CF}$ for MOR and OER in 1 M KOH

(pH = 13.9) and 1 M KOH + 4 M CH_3OH (pH = 13.7) solutions. **f** ^1H NMR spectra of products after MOR at various applied potentials. **g** HCOO^- FEs of $\text{Cu}_{\text{SA}}\text{-Rh MAS/CF}$ at various applied potentials in 1 M KOH + 4 M CH_3OH (pH = 13.7) solutions. **h** HCOO^- FEs of $\text{Cu}_{\text{SA}}\text{-Rh MAS/CF}$ at 1.4 V (vs RHE) measured for 5 successive cycles in 1 M KOH + 4 M CH_3OH (pH = 13.7) solutions.

vs RHE) and the Tafel slope value of MOR (126 mV dec^{-1}) is also smaller than that of OER (189 mV dec^{-1}) (Fig. 4d, e), indicating the thermodynamic favorability of MOR over OER owing to faster kinetics and smaller oxidation potential. To further investigate the products of the anodic MOR on $\text{Cu}_{\text{SA}}\text{-Rh MAS/CF}$, the i - t measurements were performed at various applied potentials and the electrolyzed products were analyzed via the nuclear magnetic resonance (NMR) spectra. As presented in Fig. 4f, the key value-added chemical HCOO^- is produced during the MOR process, and the HCOO^- concentration gradually increases with higher anodic applied potential. Figure 4g presents that the HCOO^- Faradaic efficiencies (FEs) for $\text{Cu}_{\text{SA}}\text{-Rh MAS/CF}$ reaches over 90% at various applied potentials (1.35–1.55 V vs RHE), where the HCOO^- FE of $\text{Cu}_{\text{SA}}\text{-Rh MAS/CF}$ is ~96.5% at 1.5 V (vs RHE), which reveals the excellent selectivity for the conversion of CH_3OH to HCOO^- on $\text{Cu}_{\text{SA}}\text{-Rh MAS/CF}$. Moreover, the ^{13}C NMR spectra of the electrolyzed products after 24 h MOR further indicate the superior HCOO^- selectivity for $\text{Cu}_{\text{SA}}\text{-Rh MAS/CF}$ and the generated CO_3^{2-} as a by-product is almost negligible (Supplementary Fig. 16). It is worth mentioning that the $\text{Cu}_{\text{SA}}\text{-Rh MAS/CF}$ possesses a superior MOR activity compared with Rhene-CF, Rh NPs-CF and CF (Supplementary Fig. 17a). Meanwhile, relative to the

standard potential (0.103 V vs RHE) of MOR¹⁷, the overpotential of $\text{Cu}_{\text{SA}}\text{-Rh MAS/CF}$ is 1.25 V (vs RHE) for reaching a current density of 20 mA cm^{-2} , which is lower than those of Rhene-CF (1.30 V vs RHE), Rh NPs-CF (1.31 V vs RHE) and CF (1.35 V vs RHE) (Supplementary Fig. 17b). Additionally, the MOR stability of $\text{Cu}_{\text{SA}}\text{-Rh MAS/CF}$ was evaluated by the repeated i - t tests under a constant potential. Figure 4h shows that the $\text{Cu}_{\text{SA}}\text{-Rh MAS/CF}$ consistently maintains the HCOO^- FEs as high as ~90% during the five repeated cycles testing, indicating excellent stability for HCOO^- production on $\text{Cu}_{\text{SA}}\text{-Rh MAS/CF}$. To investigate the charge transfer kinetics at the electrocatalytic interface, Electrochemical impedance spectroscopy (EIS) for various electrocatalysts was recorded in a 1 M KOH solution. As displayed in Supplementary Fig. 18, the $\text{Cu}_{\text{SA}}\text{-Rh MAS/CF}$ (1.13Ω) presents a smaller resistance (R_{ct}) value than Rhene-CF (1.96Ω), Rh NPs-CF (3.34Ω) and CF (9.68Ω), revealing a rapid interfacial charge transfer on $\text{Cu}_{\text{SA}}\text{-Rh MAS/CF}$ ^{52,53}. Besides, the electrochemical active surface areas (ECSAs) for various electrocatalysts were evaluated by the electrochemical double-layer capacitance (C_{dl}) calculated based on cyclic voltammetry (CV) curves (Supplementary Fig. 19). The C_{dl} value for $\text{Cu}_{\text{SA}}\text{-Rh MAS/CF}$ (49.9 mF cm^{-2}) was calculated to be higher than those of Rhene-CF (35.9 mF cm^{-2}), Rh NPs-CF (17.1 mF cm^{-2}) and

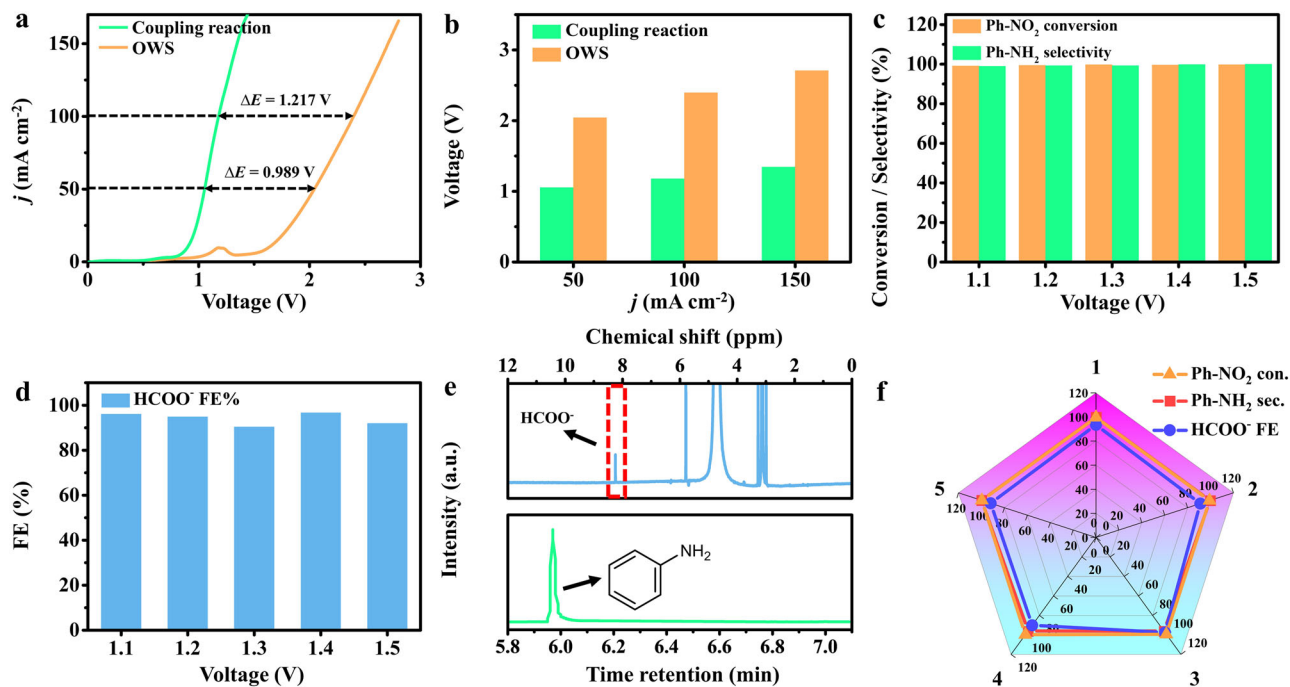


Fig. 5 | Electrochemical performance of Ph-NO₂ ERR-MOR system. **a** IR-corrected LSV curves and **b** corresponding voltages comparison for Cu_{SA}-Rh MAS/CF||Cu_{SA}-Rh MAS/CF (2.5 mg cm⁻²) in the coupled Ph-NO₂ ERR-MOR system (cathode: 1 M KOH + 5 mM Ph-NO₂ solution, pH = 13.7 and anode: 1 M KOH + 4 M CH₃OH solution, pH = 13.7) and overall water splitting system (OWS, cathode and anode: 1 M KOH solutions, pH = 13.9). **c** Ph-NO₂ conversion and Ph-NH₂ selectivity for Cu_{SA}-Rh MAS/

CF||Cu_{SA}-Rh MAS/CF under various potentials at the cathode. **d** HCOO⁻ FEs for Cu_{SA}-Rh MAS/CF||Cu_{SA}-Rh MAS/CF under various potentials at the anode. **e** GC result of products for cathodic Ph-NO₂ ERR and ¹H NMR spectra of products for anodic MOR over Cu_{SA}-Rh MAS/CF||Cu_{SA}-Rh MAS/CF at 1.2 V. **f** Ph-NO₂ conversion, Ph-NH₂ selectivity and HCOO⁻ FEs for Cu_{SA}-Rh MAS/CF||Cu_{SA}-Rh MAS/CF during the coupled reaction at 1.2 V measured for 5 successive cycles.

CF (2.1 mF cm⁻²) (Supplementary Fig. 20), which reveals the rich active sites in Cu_{SA}-Rh MAS/CF due to the ultrathin metallene array structure and the introduction of isolated Cu single-atom.

Electrocatalytic performance for Ph-NO₂ ERR-MOR system

Inspired by the above results of two half-reactions, a two-electrode system (Ph-NO₂ ERR-MOR) was constructed by employing the Cu_{SA}-Rh MAS/CF as cathode and anode. The constructed coupling system enables the simultaneous conversion of organic small molecules to targeted high-value-added chemicals and greatly optimizes energy efficiency. As shown in Fig. 5a, LSV curves of Cu_{SA}-Rh MAS/CF||Cu_{SA}-Rh MAS/CF were recorded in the Ph-NO₂ ERR-MOR system and overall water splitting (OWS) system. Apparently, the Ph-NO₂ ERR-MOR system is driven requiring a lower onset potential compared with OWS, indicating a faster reaction kinetics. The cell voltages (1.05, 1.18, and 1.35 V) of Ph-NO₂ ERR-MOR system are lower than OWS system (2.04, 2.40, and 2.71 V) at current densities of 50, 100, and 150 mA cm⁻² (Fig. 5b), revealing the improved electrolysis efficiency and lower electrolysis energy consumption in the Ph-NO₂ ERR-MOR system. For evaluating the selectivity and activity of Cu_{SA}-Rh MAS/CF||Cu_{SA}-Rh MAS/CF in the Ph-NO₂ ERR-MOR system, the electrolyzed products of cathode and anode were collected and analyzed at various applied potentials. As presented in Fig. 5c, d, the cathodic Ph-NO₂ conversion and Ph-NH₂ selectivity are up to ~100% as well and the anodic HCOO⁻ FEs also reaches over ~90% under various applied potentials, which indicates the efficient and selective targeted production of Ph-NH₂ and HCOO⁻ at cathode and anode. Furthermore, almost no by-products are generated in the Ph-NO₂ ERR-MOR coupling reaction of Cu_{SA}-Rh MAS/CF||Cu_{SA}-Rh MAS/CF (Fig. 5e). More encouragingly, the Ph-NO₂ conversion/Ph-NH₂ selectivity/HCOO⁻ FE of Cu_{SA}-Rh MAS/CF||Cu_{SA}-Rh MAS/CF remain stable after 5 repeated cycles testing in the Ph-NO₂ ERR-MOR system (Fig. 5f). Furthermore, after stability testing, no significant degradation is observed for the morphology and structure of

Cu_{SA}-Rh MAS/CF (Supplementary Fig. 21a, b), and the crystal structure of Cu_{SA}-Rh MAS remains stable (Supplementary Fig. 21c, d). Notably, Supplementary Fig. 22 further reveals that the elemental composition and chemical state of Cu_{SA}-Rh MAS show no significant change after stability testing. These conclusions indicate superior stability for the Ph-NO₂ ERR-MOR coupling system constructed by the Cu_{SA}-Rh MAS/CF.

DFT calculations

To further reveal the electronic structure effect between the isolated Cu single-atom and Rh host as well as the mechanism of enhanced electrocatalytic activity on Cu_{SA}-Rh MAS/CF, DFT calculations were carried out. Supplementary Fig. 23 shows an optimized geometric structure model for Cu_{SA}-Rh MAS. Based on the Bader charge calculation analysis (Supplementary Fig. 24 and Supplementary Table 2), the total net charges of Rh and Cu are 1.94 e and -1.94 e, respectively, which reveals that the electron transfer is from the Cu single-atom to the Rh host. Fig. 6a, b and Supplementary Fig. 25 reveal the accumulation of negative charge around the Rh host while Cu single-atom possesses positive charge property due to the loss of charge, which further indicate the electron-rich nature of Rh localization resulting from the introduction of isolated Cu single-atom. The projected partial density of states (PDOSs) of Cu_{SA}-Rh MAS show the strong overlapping of the Rh-4d orbital with the Cu-3d orbital (Fig. 6c), revealing the effective site-to-site electron transfer between the isolated Cu single-atom and the Rh host, which contributes to the optimization of electronic structures thus facilitating electrocatalytic reactions^{54,55}. Moreover, as displayed in Fig. 6d, the d-band center of Rh-4d orbitals for Cu_{SA}-Rh (111) (-1.79 eV) exhibits a slight negative shift compared with Rh (111) (-1.77 eV). It is notable that the PDOS for Rh-4d of Cu_{SA}-Rh bulk (-1.82 eV) and Rh bulk (-1.49 eV) also reflect a similar trend (Supplementary Fig. 26). As shown in Supplementary Fig. 27 and

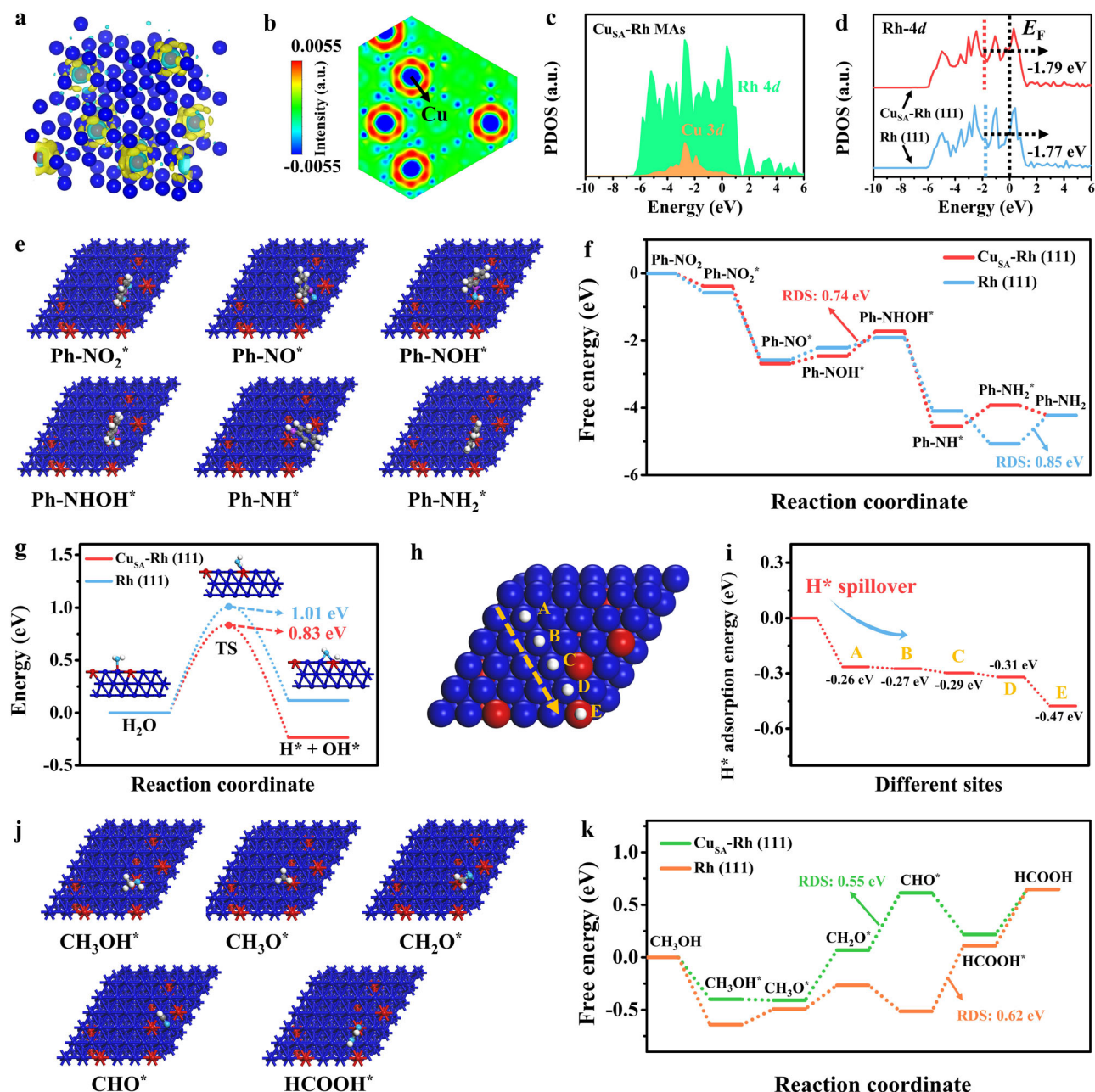


Fig. 6 | DFT calculations analysis. **a** Charge density difference on $\text{Cu}_{\text{SA}}\text{-Rh}$ model. The blue and red spheres represent Rh and Cu atoms respectively, as well as the yellow and cyan indicate the charge depletion and accumulation areas. **b** Slice of charge density difference for $\text{Cu}_{\text{SA}}\text{-Rh}$ bulk structure. **c** The PDOSs of $\text{Cu}_{\text{SA}}\text{-Rh}$. **d** The PDOSs for Rh-4d of Rh (111) and $\text{Cu}_{\text{SA}}\text{-Rh}$ (111) surfaces. **e** Optimized structures of Ph- NO_2 ERR intermediates on $\text{Cu}_{\text{SA}}\text{-Rh}$ (111). The blue, red, gray, cyan, purple, and white spheres represent Rh, Cu, C, O, N, and H atoms respectively. **f** Comparison of free energy profiles for Ph- NO_2 ERR pathway on $\text{Cu}_{\text{SA}}\text{-Rh}$ (111) and

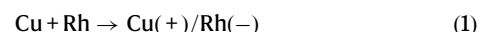
Rh (111). **g** Calculated energy profiles of H_2O dissociation on $\text{Cu}_{\text{SA}}\text{-Rh}$ (111) and Rh (111). **h** Optimized structures of adsorbed H^* and **i** calculated H^* adsorption energies variations at different sites on $\text{Cu}_{\text{SA}}\text{-Rh}$ (111). The blue, red, and white spheres represent Rh, Cu, and H atoms respectively. **j** Optimized structures of MOR intermediates on $\text{Cu}_{\text{SA}}\text{-Rh}$ (111). The blue, red, gray, cyan, and white spheres represent Rh, Cu, C, O, and H atoms respectively. **k** Comparison of free energy profiles for MOR pathway on $\text{Cu}_{\text{SA}}\text{-Rh}$ (111) and Rh (111).

Supplementary Table 3, The electron transfer between $\text{Cu}_{\text{SA}}\text{-Rh}$ and Ph- NO_2^* (0.19 e) is smaller than that between Rh and Ph- NO_2^* (0.25 e) owing to the electron interaction between Cu single-atom and the Rh host, which eventually can induce the decrease of electron interaction between $\text{Cu}_{\text{SA}}\text{-Rh}$ and Ph- NO_2^* , thus weakening the binding of Ph- NO_2^* on $\text{Cu}_{\text{SA}}\text{-Rh}$ ⁴³. Notably, there is electron accumulation in the antibonding orbitals for both $\text{Cu}_{\text{SA}}\text{-Rh}$ and Rh, which favors the weakening of the bond energy for the N-O bond^{43,56}. These conclusions indicate that the electron interaction between the isolated Cu single-atom and the Rh host causes a downshift of

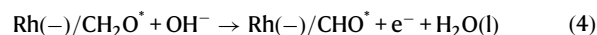
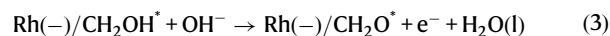
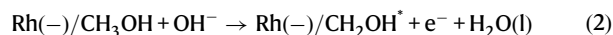
the *d*-band center and a decrease in the electron interaction between the catalyst and adsorbate, thus promoting a fast conversion of the reactants to key intermediates as well as optimizing the desorption of the target product^{8,43}. Moreover, Supplementary Fig. 28a and Supplementary Table 4 present the optimized adsorption structure and adsorption energy (ΔE_{ads}) of Ph- NO_2 on Rh (111) and $\text{Cu}_{\text{SA}}\text{-Rh}$ (111) surfaces. The calculated Ph- NO_2 ΔE_{ads} of $\text{Cu}_{\text{SA}}\text{-Rh}$ (111) is -1.08 eV, which is lower than that of Rh (111) (-1.27 eV). The weakened ΔE_{ads} of Ph- NO_2 on $\text{Cu}_{\text{SA}}\text{-Rh}$ is beneficial for the rapid conversion of Ph- NO_2 to Ph- NOOH^* by coupling with

the protons in H₂O, and the unstable Ph-NOOH* rapidly removes OH* to further form the stable and important intermediate Ph-NO*, thus enhancing the rapid protonation in the Ph-NO₂ ERR process⁸. Notably, Supplementary Fig. 28b and Supplementary Table 4 show that the Δ*E*_{ads} of the key intermediate Ph-NO* on Cu_{SA}-Rh (111) (-1.34 eV) is higher than that of Rh (111) (-1.28 eV), indicating that the intermediate Ph-NO* remains stable on Cu_{SA}-Rh and can be steadily converted to Ph-NOH* thus reducing the desorption of Ph-NO* to avoid the generation of undesired by-product azobenzene. Moreover, the free energy profiles of optimized intermediates for Ph-NO₂ ERR pathway reveal Ph-NOH*→Ph-NHOH* and Ph-NH₂*→Ph-NH₂ as the rate-determining step (RDS) for Cu_{SA}-Rh and Rh, respectively (Fig. 6e, f and Supplementary Fig. 29). Obviously, the Cu_{SA}-Rh exhibits a lower energy barrier (0.74 eV) on the RDS compared with Rh (0.85 eV) (Fig. 6f and Supplementary Table 5), further indicating the higher ability on Cu_{SA}-Rh for driving the Ph-NO₂ ERR to Ph-NH₂. To further investigate the enhanced mechanism of activity during the Ph-NO₂ hydrogenation with H₂O as the hydrogen source on Cu_{SA}-Rh MAs, a series of DFT calculations were performed and analyzed. Figure 6g and Supplementary Fig. 30 display the calculated energy profiles of H₂O dissociation process and corresponding optimized structures of the initial, transition, and final states. The energy barrier for H₂O dissociation of Cu_{SA}-Rh (0.83 eV) is lower than that of Rh (1.01 eV) (Fig. 6g and Supplementary Table 6), indicating that the introduction of the Cu single-atom is beneficial for the dissociation of H₂O on Cu_{SA}-Rh to facilitate the formation H* for Ph-NO₂ hydrogenation. Furthermore, the H* Δ*E*_{ads} of various sites (A to E) were further calculated for investigating the hydrogenation mechanism of H* with H₂O as the hydrogen source on Cu_{SA}-Rh MAs (Fig. 6h, i). Visually, the variation of H* Δ*E*_{ads} from A to E sites on Cu_{SA}-Rh reveals a gradually increased H* adsorption (Fig. 6i and Supplementary Table 7), which indicates a H*-spillover process between the isolated Cu single-atom and the Rh host. This can be ascribed to local adsorption differences induced by electronic effect of Cu single-atom and Rh host. In the H*-spillover process (Supplementary Fig. 31), the formed H* from H₂O dissociation on Rh host can spontaneously and rapidly migrate on the isolated Cu single-atom thus stabilizing H* for the hydrogenation process of intermediates, which is beneficial for inhibiting competing reaction HER and avoiding the H* accumulation on the Rh host to occupy the active sites thus maximizing the utilization of H* to promote synergistic electrocatalytic effects on Cu single-atom and Rh host for Ph-NO₂ ERR. For further investigating the MOR mechanism on Cu_{SA}-Rh MAs, the free energy profiles of optimized intermediates for MOR pathway were analyzed by the DFT calculations (Fig. 6j, k and Supplementary Fig. 32). It can be observed that the Cu_{SA}-Rh possesses a lower energy barrier for RDS (CH₂O* → CHO*, 0.55 eV) compared to the RDS (CHO* → HCOOH*, 0.62 eV) of Rh (Fig. 6k and Supplementary Table 8), indicating a more favorable MOR process on Cu_{SA}-Rh. Additionally, the CH₃OH-to-HCOO⁻ is regarded as a continuous dehydrogenation process of CH₃OH, and the adsorption of the key intermediate CHO* is critical for the HCOO⁻ synthesis. As shown in Supplementary Fig. 33 and Supplementary Table 9, the Δ*E*_{ads} of CHO* for Cu_{SA}-Rh (111) (-5.09 eV) is lower than that for Rh (111) (-5.33 eV). Meanwhile, Fig. 6k further shows that the energy barrier for the desorption step (HCOOH* → HCOOH) of Cu_{SA}-Rh (0.43 eV) is lower than that of Rh (0.54 eV). These conclusions reveal that the introduction of Cu single-atom can effectively reduce the Δ*E*_{ads} of key intermediate CHO* leading to the easier desorption of the target product from the Cu_{SA}-Rh MAs surface, which is conducive to facilitating the HCOO⁻ formation and avoiding the unnecessary oxidation process. Moreover, the MOR mechanism on Cu_{SA}-Rh was speculated as illustrated in Supplementary Fig. 34. Due to the electron effect between Cu and Rh, the electron transfer from the Cu single-atom to Rh host

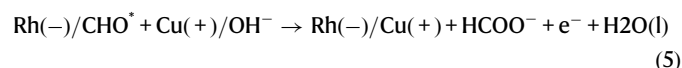
can activate electron-rich Rh (reaction 1).



Initially, The CH₃OH tends to adsorb on the electron-rich Rh (reaction 2), and then the CHO* is produced through a series of dehydrogenation reactions on Cu_{SA}-Rh (reactions 3 and 4).



Finally, the HCOO⁻ is produced by nucleophilic attack of OH⁻ adsorbed around the positively charged Cu against the electrophilic carbocation in CHO* and rapidly desorbs owing to the weak adsorption energy of CHO* (reaction 5).



Based on the above conclusion analysis, the superior Ph-NO₂ ERR and MOR activity of Cu_{SA}-Rh MAs/CF originates from the following points: Firstly, the stable security wall-like structure formed by the ultrathin metallene arrays provides sufficient active sites and abundant interlayer channels⁴⁵. Secondly, the inherent defect-rich structure and low-crystalline regions of Cu_{SA}-Rh MAs/CF can induce unsaturated coordination metallic bonds and optimize the local electron structure^{37,56}. Thirdly, the synergistic catalysis effect and H*-spillover effect between Cu single-atom and Rh host can optimize the catalytic reaction process, facilitate the stable and rapid conversion of reactants to intermediates as well as accelerate the desorption of target products. Fourthly, the Cu single-atom as effective adsorption sites can modulate the competition for adsorbate adsorption on Rh sites thus promoting electrocatalytic reactions.

Discussion

In summary, we have successfully synthesized the Cu_{SA}-Rh MAs/CF with the isolated Cu single-atom dispersed on Rh metallene that possesses excellent electrocatalytic activity towards Ph-NO₂ ERR and MOR. The Cu_{SA}-Rh MAs/CF exhibits the low cell voltages (1.05 and 1.18 V) to achieve the current densities of 50 and 100 mA cm⁻² in the Ph-NO₂ ERR-MOR coupled system, and the cathodic Ph-NO₂ conversion/Ph-NH₂ selectivity are up to -100% as well as the anodic HCOO⁻ FEs also reaches over -90%. The constructed coupled organic electrocatalytic conversion system achieves simultaneous conversion of low-value organic compounds to high-value chemicals at both cathode and anode as well as improves energy efficiency. The electron effect between Cu single-atom and Rh host and the catalytic reaction mechanism were further revealed by DFT calculations, in which the synergistic catalytic effect and H*-spillover effect are triggered by the local electronic structure change between the Cu single-atom and Rh host, which optimizes the catalytic reaction process and facilitate the rapid production of key intermediates and the rapid desorption of target products. This work provides a novel strategy for the design of SAAs catalysts applied in the sustainable green synthesis of high-value chemicals.

Methods

Materials and chemicals

Cu foam (CF) was provided from Changsha Lyrun Material Co., Ltd. Rhodium (II) acetate dimer (C₈H₁₂O₈Rh₂, Rh: 43–46%), rhodium

chloride (RhCl₃, 98%), potassium hydroxide (KOH, AR, 85%), methanol (CH₃OH, AR, 99.5%), ethylene glycol (EG, AR, 99%), N,N-dimethylformamide (DMF, AR, 99.5%), diethylenetriamine (DETA, AR, 99%) and maleic acid (≥99%) were purchased from Aladdin Industrial Corporation (China). Ethyl acetate (99%), nitrobenzene (Ph-NO₂, AR, 99%) and aniline (Ph-NH₂, ≥99.5%) were ordered from Shanghai Macklin Biochemical Co., Ltd. (China). Ethanol (C₂H₅OH, 95%) and hydrochloric acid (HCl, 37%) were acquired from Sinopharm Chemical Reagent Co., Ltd. (China). High-purity Ar gas (99.99%) was obtained from Hangzhou Special Gases Co., Ltd. (China).

Synthesis of Cu_{SA}-Rh MAs/CF

For a typical synthesis of Cu_{SA}-Rh MAs/CF, the 1 × 2 cm² of CF was soaked in a 3 M HCl solution for 20 min, followed by washing several times with ethanol/water, and then dried at 50 °C in a vacuum oven for further utilization. Typically, 10 mg of C₈H₁₂O₈Rh₂ and 1 g of KOH were ultrasonically dissolved in a mixture of DMF (6 mL) and EG (4 mL). Then, 5 mL of DETA was dropped into the above solution to form a homogeneous solution, the obtained solution was transferred into a 25 mL Teflon-lined autoclave and the treated CF was placed into the autoclave. Afterward, the autoclave was heated to 200 °C and kept for 8 h. After naturally cooling to room temperature, the product was extracted from the autoclave and washed several times with water/ethanol. Finally, the product was dried in a vacuum oven at 60 °C for further characterization and electrochemical measurements.

Synthesis of Rhene-CF

For a typical synthesis of Rhene-CF, 1 g of KOH and 10 mg of C₈H₁₂O₈Rh₂ were dissolved in a 30 mL vial containing 6 mL of DMF and 4 mL of EG. Then, 5 mL of DETA was slowly added to the above solution to form a homogeneous solution. The obtained solution was transferred to a 25 mL of Teflon-lined autoclave, followed by heating to 200 °C and maintaining for 1 h. After that, the product was obtained by centrifuging and washing several times with water/ethanol and dried in a vacuum oven at 60 °C for further utilization. Finally, the Rhene-CF was prepared by covering the prepared Rhene on CF.

Synthesis of Rh NPs-CF

For a typical synthesis of Rh NPs-CF, 10 mg of RhCl₃ was dissolved in 30 mL of EG to form a homogeneous solution. The above solution was transferred to a 50 mL Teflon-lined autoclave and heated at 200 °C for 2 h. Then, the product was collected by centrifuging and washing several times with water/ethanol and dried in a vacuum oven at 60 °C for further utilization. Finally, the Rh NPs-CF was prepared by covering the prepared Rh NPs on CF.

Material characterizations

Scanning electron microscopy (SEM) images were collected on a Zeiss Gemini 500. TEM images and selected area electron diffraction (SAED) data were collected on an FEI Tecnai G2 F30 (300 kV). Aberration-corrected high angle annular dark field scanning transmission electron microscopy (AC-HAADF-STEM) images, EELS, and elemental mapping data were collected on a Thermo Scientific Themis Z. Atomic force microscopy (AFM) was conducted on a Bruker Multimode 8. XRD data were recorded with a PANalytical Empyrean powder diffractometer using Cu K α radiation and XPS data were collected on a Thermo ESCALAB 250XI. Rh *K*-edge and Cu *K*-edge XANES and EXAFS data were acquired from a BL14W1 beamlines at the Shanghai Synchrotron Radiation Facility (Shanghai, China). The inductively coupled plasma optical emission spectroscopy (ICP-OES) data were collected from a PerkinElmer ICP 2100. Nuclear magnetic resonance (NMR) spectra were collected on a Bruker Avance NEO 600 and gas chromatograph (GC) was conducted on an Agilent 8890/7000D.

Electrochemical experiments

Electrochemical measurements were conducted on a CHI760E electrochemical workstation (Shanghai Chenhua Instrument Corporation, China) via a two/three-electrode system, where contains the reference electrode (Hg/HgO electrode), counter electrode (Pt foil and carbon rod), and working electrode. As a blinder-free electrode, the Cu_{SA}-Rh MAs/CF can be directly used as a working electrode, where Rhene-CF, Rh NPs-CF and CF serve as the comparison. Regarding cathodic Ph-NO₂ electroreduction reaction (Ph-NO₂ ERR), all electrochemical tests were conducted in an H-type cell with the Nafion 117 membrane separation, where the cathode chamber contains working electrodes and Hg/HgO electrode, and the anode chamber contains Pt foil. The cathode and anode electrolytes were a 1 M KOH + 5 mM Ph-NO₂ solution and a 1 M KOH solution, respectively. Before the Ph-NO₂ ERR test, Ar gas (99.99%) was continuously passed into the cathode chamber to purify the electrolyte for 20 min. More importantly, the cathode chamber needs to be continuously flooded with Ar gas during the whole Ph-NO₂ ERR tests. Regarding anodic methanol oxidation reaction (MOR), electrochemical tests were conducted in a single-chamber cell via a three-electrode system containing a working electrode, reference electrode (Hg/HgO electrode), and counter electrode (carbon rod). Regarding Ph-NO₂ ERR-MOR two-electrode system, the Cu_{SA}-Rh MAs/CF served as the cathode and anode electrodes, respectively. The cathode and anode electrolytes were a 1 M KOH + 5 mM Ph-NO₂ solution and a 1 M KOH + 4 M CH₃OH solution, respectively. All linear sweep voltammetry (LSV) curves were recorded at a scan rate of 5 mV s⁻¹ with 95% iR-compensation, and the current density for Ph-NO₂ ERR and MOR was acquired by normalizing to the geometric area of the CF. The applied potentials are converted into reversible hydrogen electrode (RHE) scale according to the Eq. (6):

$$E(\text{vs. RHE}) = E^{\theta}(\text{Hg/HgO}) + E(\text{vs. Hg/HgO}) + 0.059 \times \text{pH}. \quad (6)$$

EIS was carried out in the range of 0.1 Hz to 100 kHz.

Product analysis

For Ph-NO₂ ERR, the electrolyte was collected and extracted with ethyl acetate after *i-t* tests. The extracted products were determined by comparing the GC retention times and mass spectra. The Ph-NO₂ conversion and Ph-NH₂ selectivity were acquired via the GC results analysis and calculated based on the following Eqs. (7) and (8):

$$\text{Conversion} = \frac{\text{mol of the consumed Ph-NO}_2}{\text{mole of the added Ph-NO}_2} \times 100\% \quad (7)$$

$$\text{Selectivity} = \frac{\text{mol of the as-formed Ph-NH}_2}{\text{mole of the added Ph-NO}_2} \times 100\% \quad (8)$$

For MOR, the electrolyte after *i-t* tests was collected and analyzed via the NMR spectroscopy, where maleic acid served as an internal standard. The HCOO⁻ FEs were calculated based on the following Eq. (9):

$$FE(\text{HCOO}^-) = \frac{N(\text{Production}) \times Z \times F}{Q} \times 100\% \quad (9)$$

Where *N* is the molar amount for the formed HCOO⁻, *Z* is the number of electrons transferred for the formed HCOO⁻ (*Z* = 4), *F* is the Faraday constant (96485 C mol⁻¹), *Q* is the total amount of charge consumed.

Computational methods

Details of the calculation method can be found in the Supplementary method.

Data availability

The authors declare that all data supporting the findings of this study are available within the article and its Supplementary Information. The source data generated in this study are available in the figshare repository (<https://doi.org/10.6084/m9.figshare.23994690.v1>).

References

1. Akhade, S. A. et al. Electrocatalytic hydrogenation of biomass-derived organics: a review. *Chem. Rev.* **120**, 11370–11419 (2020).
2. Yang, G. et al. Unraveling the mechanism for paired electrocatalysis of organics with water as a feedstock. *Nat. Commun.* **13**, 3125 (2022).
3. Von Munchow, T., Dana, S., Xu, Y., Yuan, B. & Ackermann, L. Enantioselective electrochemical cobalt-catalyzed aryl C-H activation reactions. *Science* **379**, 1036–1042 (2023).
4. Yang, M., Yuan, Z. R., Peng, R. X., Wang, S. Y. & Zou, Y. Q. Recent progress on electrocatalytic valorization of biomass-derived organics. *Energy Environ. Mater.* **5**, 1117–1138 (2022).
5. Wang, F. & Stahl, S. S. Electrochemical oxidation of organic molecules at lower overpotential: accessing broader functional group compatibility with electron-proton transfer mediators. *Acc. Chem. Res.* **53**, 561–574 (2020).
6. Meng, N. et al. Electrosynthesis of formamide from methanol and ammonia under ambient conditions. *Nat. Commun.* **13**, 5452 (2022).
7. Andrews, E. et al. Performance of base and noble metals for electrocatalytic hydrogenation of bio-oil-derived oxygenated compounds. *ACS Sustain. Chem. Eng.* **8**, 4407–4418 (2020).
8. Ma, J., Wang, Z., Majima, T. & Zhao, G. Role of Ni in PtNi alloy for modulating the proton–electron transfer of electrocatalytic hydrogenation revealed by the in situ raman–rotating disk electrode method. *ACS Catal.* **12**, 14062–14071 (2022).
9. Ahmadi, A. & Wu, T. T. Electrocatalytic reduction of nitrobenzene using TiO₂ nanotube electrodes with different morphologies: Kinetics, mechanism, and degradation pathways. *Chem. Eng. J.* **374**, 1241–1252 (2019).
10. Jin, M. et al. Selective electrocatalytic hydrogenation of nitrobenzene over copper–platinum alloying catalysts: experimental and theoretical studies. *Appl. Catal. B: Environ.* **298**, 120545 (2021).
11. Zhao, Y., Liu, C., Wang, C., Chong, X. & Zhang, B. Sulfur vacancy-promoted highly selective electrosynthesis of functionalized aminoarenes via transfer hydrogenation of nitroarenes with H₂O over a Co₃S_{4-x} nanosheet cathode. *CCS Chem.* **3**, 507–515 (2021).
12. Mao, Q. et al. Sulfur vacancy-rich amorphous Rh metallene sulfide for electrocatalytic selective synthesis of aniline coupled with efficient sulfion degradation. *ACS Nano* **17**, 790–800 (2023).
13. Forslund, R. P., Alexander, C. T., Abakumov, A. M., Johnston, K. P. & Stevenson, K. J. Enhanced electrocatalytic activities by substitutional tuning of nickel-based ruddlesden–popper catalysts for the oxidation of urea and small alcohols. *ACS Catal.* **9**, 2664–2673 (2019).
14. Ge, R. et al. Selective electrooxidation of biomass-derived alcohols to aldehydes in a neutral medium: promoted water dissociation over a nickel-oxide-supported ruthenium single-atom catalyst. *Angew. Chem. Int. Ed.* **61**, 202200211 (2022).
15. Zhao, H. et al. Raw biomass electroreforming coupled to green hydrogen generation. *Nat. Commun.* **12**, 2008 (2021).
16. Begildayeva T. et al. Sustainable furfural biomass feedstocks electrooxidation toward value-added furoic acid with energy-saving H₂ fuel production using Pt-decorated Co₃O₄ nanospheres. *Energy Environ. Mater.* e12563 <https://doi.org/10.1002/eeem2.12563> (2023).
17. Zhu, B. et al. Unraveling a bifunctional mechanism for methanol-to-formate electro-oxidation on nickel-based hydroxides. *Nat. Commun.* **14**, 1686 (2023).
18. Li, S. et al. Coordination environment tuning of nickel sites by oxyanions to optimize methanol electro-oxidation activity. *Nat. Commun.* **13**, 2916 (2022).
19. Hao, J. et al. In situ facile fabrication of Ni(OH)₂ nanosheet arrays for electrocatalytic co-production of formate and hydrogen from methanol in alkaline solution. *Appl. Catal. B: Environ.* **281**, 119510 (2021).
20. Xiang, K. et al. Boosting H₂ generation coupled with selective oxidation of methanol into value-added chemical over cobalt hydroxide@hydroxysulfide nanosheets electrocatalysts. *Adv. Funct. Mater.* **30**, 1909610 (2020).
21. Daems, N. et al. Selective reduction of nitrobenzene to aniline over electrocatalysts based on nitrogen-doped carbons containing non-noble metals. *Appl. Catal. B: Environ.* **226**, 509–522 (2018).
22. Yang, Q. F. et al. Synergistic modulation of nanostructure and active sites: Ternary Ru&Fe-WO_x electrocatalyst for boosting concurrent generations of hydrogen and formate over 500 mA cm⁻². *Appl. Catal. B: Environ.* **296**, 120359 (2021).
23. Giannakakis, G. et al. Mechanistic and electronic insights into a working NiAu single-atom alloy ethanol dehydrogenation catalyst. *J. Am. Chem. Soc.* **143**, 21567–21579 (2021).
24. Kyriakou, G. et al. Isolated metal atom geometries as a strategy for selective heterogeneous hydrogenations. *Science* **335**, 1209–1212 (2012).
25. Shen, T., Wang, S., Zhao, T. H., Hu, Y. Z. & Wang, D. L. Recent advances of single-atom-alloy for energy electrocatalysis. *Adv. Energy Mater.* **12**, 2201823 (2022).
26. Hannagan, R. T., Giannakakis, G., Flytzani-Stephanopoulos, M. & Sykes, E. C. H. Single-atom alloy catalysis. *Chem. Rev.* **120**, 12044–12088 (2020).
27. Liu, W. et al. Highly-efficient RuNi single-atom alloy catalysts toward chemoselective hydrogenation of nitroarenes. *Nat. Commun.* **13**, 3188 (2022).
28. Mao, J. et al. Isolated Ni atoms dispersed on Ru nanosheets: high-performance electrocatalysts toward hydrogen oxidation reaction. *Nano Lett.* **20**, 3442–3448 (2020).
29. Wu, X. et al. Contrasting capability of single atom palladium for thermocatalytic versus electrocatalytic nitrate reduction reaction. *ACS Catal.* **13**, 6804–6812 (2023).
30. Lee, J. et al. Stabilizing the OOH* intermediate via pre-adsorbed surface oxygen of a single Ru atom-bimetallic alloy for ultralow overpotential oxygen generation. *Energy Environ. Sci.* **13**, 5152–5164 (2020).
31. Ji, K. et al. Electrocatalytic hydrogenation of 5-hydroxymethylfurfural promoted by a Ru₁Cu single-atom alloy catalyst. *Angew. Chem. Int. Ed.* **61**, 202209849 (2022).
32. Li, X. et al. PdFe single-atom alloy metallene for N₂ electroreduction. *Angew. Chem. Int. Ed.* **61**, 202205923 (2022).
33. Luo, S. et al. A tensile-strained Pt-Rh single-atom alloy remarkably boosts ethanol oxidation. *Adv. Mater.* **33**, 2008508 (2021).
34. Li, M. et al. Single-atom tailoring of platinum nanocatalysts for high-performance multifunctional electrocatalysis. *Nat. Catal.* **2**, 495–503 (2019).
35. Prabhu, P. et al. Oxygen-bridged stabilization of single atomic W on Rh metallenes for robust and efficient pH-universal hydrogen evolution. *ACS Nano* **17**, 10733–10747 (2023).
36. Yu, H. et al. Defect-rich porous palladium metallene for enhanced alkaline oxygen reduction electrocatalysis. *Angew. Chem. Int. Ed.* **60**, 12027–12031 (2021).
37. Prabhu, P. & Lee, J. M. Metallenes as functional materials in electrocatalysis. *Chem. Soc. Rev.* **50**, 6700–6719 (2021).
38. Luo, M. et al. PdMo bimetallic for oxygen reduction catalysis. *Nature* **574**, 81–85 (2019).
39. Mao, Q. et al. Low-content Pt-triggered the optimized d-band center of Rh metallene for energy-saving hydrogen production coupled with hydrazine degradation. *J. Energy Chem.* **85**, 58–66 (2023).

40. Do, V. H. et al. Pd-PdO nanodomains on amorphous Ru metallene oxide for high-performance multifunctional electrocatalysis. *Adv. Mater.* **35**, 2208860 (2023).
41. Li, X., Shen, P., Li, X., Ma, D. & Chu, K. Sub-nm RuO_x clusters on Pd metallene for synergistically enhanced nitrate electroreduction to ammonia. *ACS Nano* **17**, 1081–1090 (2023).
42. Wu, J. et al. Atomically dispersed MoO_x on Rhodium metallene boosts electrocatalyzed alkaline hydrogen evolution. *Angew. Chem. Int. Ed.* **61**, 202207512 (2022).
43. Chen, K. et al. Single-atom Bi alloyed Pd metallene for nitrate electroreduction to ammonia. *Adv. Funct. Mater.* **33**, 2209890 (2023).
44. Yang, Q. et al. Facile synthesis of ultrathin Pt-Pd nanosheets for enhanced formic acid oxidation and oxygen reduction reaction. *J. Mater. Chem. A* **7**, 18846–18851 (2019).
45. Babar, P. et al. Bifunctional 2D electrocatalysts of transition metal hydroxide nanosheet arrays for water splitting and urea electrolysis. *ACS Sustain. Chem. Eng.* **7**, 10035–10043 (2019).
46. Li, Z. et al. Stable rhodium (IV) oxide for alkaline hydrogen evolution reaction. *Adv. Mater.* **32**, 1908521 (2020).
47. Zhong, W. et al. RhSe₂: a superior 3D electrocatalyst with multiple active facets for hydrogen evolution reaction in both acid and alkaline solutions. *Adv. Mater.* **33**, 2007894 (2021).
48. Morales, M. R. et al. In-depth structural and analytical study of the washcoating layer of a Mn-Cu monolithic catalyst using STEM-FIB, EDX and EELS. Insights into stability under working conditions. *Appl. Surf. Sci.* **563**, 150318 (2021).
49. Zhang, J. et al. Atomic-thick metastable phase RhMo nanosheets for hydrogen oxidation catalysis. *Nat. Commun.* **14**, 1761 (2023).
50. Kim, J. Y. et al. Synergistic effect of Cu₂O mesh pattern on high-facet Cu surface for selective CO₂ electroreduction to ethanol. *Adv. Mater.* **34**, 2106028 (2022).
51. Kumar, A. et al. Modulating interfacial charge density of NiP₂-FeP₂ via coupling with metallic Cu for accelerating alkaline hydrogen evolution. *ACS Energy Lett.* **6**, 354–363 (2021).
52. Wang Z. et al. Nontrivial topological surface states in Ru₃Sn₇ toward wide pH-range hydrogen evolution reaction. *Adv. Mater.* **35**, 2302007 (2023).
53. Wang, X. et al. Fabricating Ru single atoms and clusters on CoP for boosted hydrogen evolution reaction. *Chin. J. Struct. Chem.* **42**, 100035 (2023).
54. Tao, L. et al. A general synthetic method for high-entropy alloy subnanometer ribbons. *J. Am. Chem. Soc.* **144**, 10582–10590 (2022).
55. Zhan, C. et al. Subnanometer high-entropy alloy nanowires enable remarkable hydrogen oxidation catalysis. *Nat. Commun.* **12**, 6261 (2021).
56. Cao, D., Xu, H. & Cheng, D. Construction of defect-rich RhCu nanotubes with highly active Rh₃Cu₁ alloy phase for overall water splitting in all pH values. *Adv. Energy Mater.* **10**, 1903038 (2020).

Acknowledgements

This work was financially supported by the National Natural Science Foundation of China (No. 21972126, 21978264, 21905250, and 22278369), National Science Foundation of Zhejiang Province (No. LQ22B030012 and LQ23B030010), and China Postdoctoral Science Foundation (2021M702889).

Author contributions

H.W. and Q.M. conceived the idea and designed the experiments. X.M. and W.W. conducted the synthesis and characterization of samples and electrochemical experiments. H.W. and L.W. supervised the project. K.D. and L.W. analyzed the XANES and EXAFS results. Z.W. and H.Y. performed and analyzed DFT calculations. H.W. and Q.M. analyzed the results and wrote the paper. K.D. and Y.X. helped with the revision of the paper.

Competing interests

The authors declare no competing interests.

Additional information

Supplementary information The online version contains supplementary material available at <https://doi.org/10.1038/s41467-023-41423-2>.

Correspondence and requests for materials should be addressed to Hongjing Wang.

Peer review information *Nature Communications* thanks the anonymous reviewers for their contribution to the peer review of this work. A peer review file is available.

Reprints and permissions information is available at <http://www.nature.com/reprints>

Publisher's note Springer Nature remains neutral with regard to jurisdictional claims in published maps and institutional affiliations.

Open Access This article is licensed under a Creative Commons Attribution 4.0 International License, which permits use, sharing, adaptation, distribution and reproduction in any medium or format, as long as you give appropriate credit to the original author(s) and the source, provide a link to the Creative Commons licence, and indicate if changes were made. The images or other third party material in this article are included in the article's Creative Commons licence, unless indicated otherwise in a credit line to the material. If material is not included in the article's Creative Commons licence and your intended use is not permitted by statutory regulation or exceeds the permitted use, you will need to obtain permission directly from the copyright holder. To view a copy of this licence, visit <http://creativecommons.org/licenses/by/4.0/>.

© The Author(s) 2023